Proceedings of the 2020 AIAA Scitech Forum, 6-10 January, Orlando, Florida, USA
DOI:10.2514/6.2020-2222

Geometry Parametrization and Aerodynamic Characteristics of Axisymmetric Afterbodies

G. Zuccolo[1], D. MacManus[2] and I. Goulos[3]
Cranfield University, Cranfield, Bedfordshire, MK43 0AL, United Kingdom

P. Martin[4]
Defence Science and Technology Laboratory, Portsdown West, Fareham, PO17 6AD, United Kingdom

A key aspect of the preliminary design process for a new generation combat aircraft is the prediction of afterbody aerodynamic drag. Current prediction methods for preliminary design are constrained in terms of number of independent geometric degrees of freedom that can be studied due to the classic circular arc or conical afterbody geometry parametrization. In addition, the amount of data available for the construction of the reliable performance correlations is too sparse. This paper presents a methodology for the generation of aerodynamic performance maps for transonic axisymmetric afterbody and exhaust systems. It uses a novel parametric geometry definition along with a compressible flow solver to conduct an extensive design space exploration. The proposed geometry parametrization is based on the Class Shape Transformation method and it enables the assessment of the aerodynamic performance of a wider range of afterbodies at the expense of one additional geometric degree of freedom. Relative to the conventional approach, this enables the exploration of a wider design space and the construction of more complete aerodynamic performance maps. This research quantifies the impact of a number of geometric degrees of freedom on the aerodynamic performance of transonic afterbody and exhaust systems at different operating conditions.

I. Nomenclature

Roman symbols:

A_9/A_8 = nozzle exit to throat area ratio
A_1 = afterbody shoulder cross-sectional area $A_1 = \pi r_i^2$
$C_{D\theta}$ = afterbody pressure drag coefficient based on A_1 (see ref.)
C_D = afterbody drag coefficient based on A_1
C_V = exhaust velocity coefficient
L = afterbody length
M_∞ = free-stream Mach number
NPR = nozzle inlet total to static Pressure Ratio $NPR = \frac{P_7}{p_\infty}$
$DNPR$ = design point nozzle inlet total to static pressure ratio, function of A_9/A_8
R = gas constant: $R = 287\ J/Kg\ K$

[1] PhD Candidate, Centre for Propulsion Engineering, g.zuccolo@cranfield.ac.uk.
[2] Head of Gas Turbine Technology Group, Centre for Propulsion Engineering, D.G.Macmanus@cranfield.ac.uk.
[3] Lecturer in Propulsion Integration, Centre for Propulsion Engineering, i.goulos@cranfield.ac.uk.
[4] Principal Scientist, Defence Science and Technology Laboratory.

Published by AIAA. This is the Author Accepted Manuscript issued with: Creative Commons Attribution Non-Commercial License (CC:BY:NC 4.0).
The final published version (version of record) is available online at DOI:10.2514/6.2020-2222. Please refer to any applicable publisher terms of use.

Published by the American Institute of Aeronautics and Astronautics, Inc., with permission.

T_7 = nozzle inlet total temperature
NAF = net afterbody force
D_N = normalized drag force
NAF_N = net afterbody force with normalized F_9 = f (DNPR,A_9/A_8)
NAF_R = net afterbody force with normalized F_9 = f (NPR)

Greek symbols:
γ = specific heat ratio
β = boattail final closing angle
δ = nozzle base thickness, %r_9
Δ = afterbody closure ratio $r_i/(r_9 + \delta)$
ϑ = afterbody mean angle

II.Introduction

Some new generation fighter aircraft are expected to be multi-role vehicles designed to perform a variety of missions. The required flexibility makes the design process more challenging and different requirements must be taken into account over a wide range of flight Mach numbers and engine power settings. These requirements may include high manoeuvrability, low infrared signature, thrust vectoring, variable area nozzle and low radar signature as well as extended range [1]. To comply with these performance demands the integration of the propulsion system within the aircraft is a key consideration. Intakes and afterbody-nozzle systems can include moving parts to efficiently accommodate different power settings and flight speeds. In addition, due to weight, balance and internal packaging requirements, fighter-type aircraft tend to incorporate short, steep afterbodies which may be prone to external flow separation [2].

Although an aircraft has many sources of drag, not all the components contribute in the same manner. For instance, in some vehicles the afterbody can account for up to 30% of the zero-lift drag [3]. Consequently it is important to understand the afterbody drag sensitivity to geometric features, engine power settings and aircraft flight conditions. Past studies ([2], [4], [5]) have experimentally addressed the effect of M_∞, NPR and afterbody mean angle (ϑ) on drag for simple geometry parametrizations such as circular arc and conical afterbodies. These parametrizations are defined by a second order equation and a first order equation respectively. This over restricts the number of geometric Degrees of Freedom (DoF) that can be explored independently within a Design Space Exploration (DSE) to afterbody length (L) and closure ratio (Δ) and leads to sparse data that is difficult to use within a preliminary design process [6].

This study proposes a new methodology for afterbody geometry parametrization based on the Class Shape Transformation (CST) method [7], [8]. This increases the number of independent geometric DoF to three: L, ϑ and β. The performance maps are generated by means of steady compressible Computational Fluid Dynamics (CFD) simulations. Moreover, this work quantitatively assesses the benefits of the additional DoF (β) within the context of a preliminary design process.

III.Background

Conventional afterbody and nozzle systems for combat aircraft in dry cruise power settings are, in many cases, parametrized with a circular arc geometry [4]. This parametrization gives a simple analytical geometry representation method and it generates shapes with a reasonable aerodynamic drag performance and reduced length [2], [4]. A circular arc afterbody is defined with three independent geometrical constraints. These are the afterbody length (L), radial offset of the end points (r_i - r_9) and geometry slope at P_1 = [0,r_i] (Fig. 1). This uniquely defines the curve that connects P_1 to P_2 and gives no control over β. Another parametrization that has been used in the past is a conical configuration [9]. For this case the number of independent geometrical parameters needed to define the afterbody end points are reduced to afterbody length (L) and radial offset (r_i - r_9). This parametrization usually includes a gradient discontinuity at the shoulder (P_1) and does not give any control over β. In this case the closing angle equals the afterbody mean angle ($\beta = \vartheta$).

Much of the previously published information on afterbody design and aerodynamic performance is based on parametric experimental studies covering a range of radial offset and afterbody length [2], [4]. In typical wind-tunnel studies it is common practice to divide the model in forebody, centerbody and afterbody and the part instrumented for data acquisition is normally the external surface of the afterbody [10]. This enables measurements of the pressure distribution along the afterbody external contour for ranges of M_∞ and NPR. The pressure readings are integrated to

obtain pressure forces that are used to compute the pressure drag coefficient $C_{D\beta}$ [2], [4], [9], [11]. There also have been previous computational studies on afterbody and nozzle system aerodynamic performance [12]–[14]. This data was mostly used to validate numerical schemes or as a case study and it was restricted to specific areas such as internal exhaust performance. Much of the previously published work about afterbody external aerodynamic performance employs simple convergent nozzle ducts or straight-walled convergent divergent ducts (Fig. 1). This affects the exhaust flow topology resulting in complex shock structures inside the nozzle duct and it changes the static pressure downstream of the nozzle exit section. This implies that the effect of the external afterbody geometry on afterbody aerodynamic performance is affected by the exhaust flow topology.

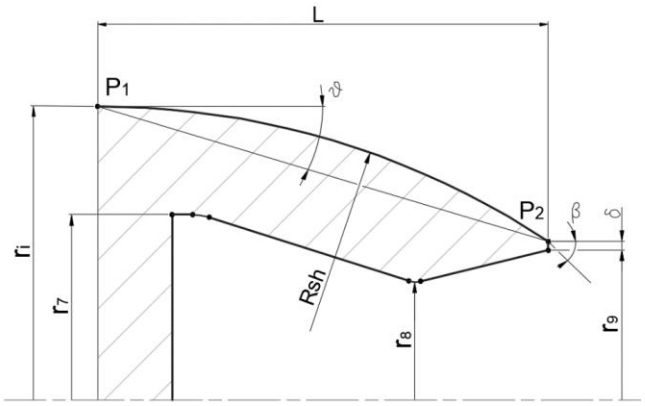


Fig. 1: Conventional afterbody geometry parametrized using a circular arc

IV.Methodology

A. Afterbody and Exhaust Parametrization

The axisymmetric afterbody parametrization is based on the CST method [7], [8]. This analytically defines geometries with desirable properties such as infinitely differentiable and continuous using an arbitrary number of intuitive Degrees of Freedom (DoF) [7] such as the location of the end points (P_3=[L_1,r_i] and P_2=[L,r_9+δ]), the slope at P_3 and the slope at P_2. In addition to the intuitive DoF some other constraints are set to improve the robustness of the geometry generation process. These are the second ($(dr^2/d^2x)_{P3}$) and third ($(dr^3/d^3x)_{P3}$) derivatives at P_3 which are both set to 0. This ensures that the shoulder of the afterbody does not overshoot and for x>x(P_3) it satisfies the condition r(x)<r_i (Fig. 2). The total number of constraints needed to define one afterbody aeroline is 6 and this gives a curve of order 5.

The internal exhaust duct is designed with the Method of Characteristics (MoC) [15], [16]. This provides the ideal nozzle contour for a given exit to throat area ratio (A_9/A_8) that gives a smooth, shock-free, parallel flow at the nozzle exit section. This produces a cylindrical stream tube of constant section that minimizes the interaction terms between the exhaust internal flow and the afterbody external flow at the design NPR (DNPR) enabling the assessment of the effect of afterbody external geometry on the afterbody aerodynamic performance. The MoC implementation was based on a second order finite difference method and it assumes calorically perfect gas [17], [18]. The MoC-based exhaust duct uses one geometrical DoF (A_9/A_8) and takes the throat radius r_8 (Fig. 3) as initial boundary condition. To assess the accuracy of the method the value of A_9/A_8 was converged within 0.005% of the input value. The convergent part of the nozzle duct has an inlet to throat area ratio equals to A_7/A_8=2.25 and was designed using a 3rd order CST. This connects point P_5[(x_{P6}-L/3),r_7] to P_6(x_{P6}, r_8) (Fig. 3). Additional constraints on the convergent nozzle duct are the slope at P_5 and the slope at P_6, which are set to 0. For CFD computational stability the point P_5 is extended horizontally for a length equals to 0.03L until intersection with the nozzle inlet. A complete afterbody and nozzle system geometry is then defined by 6 independent DoF: afterbody length (L), shoulder radius (r_i), nozzle base thickness (δ), boattail angle (β), the straight shoulder length (L_1) and A_9/A_8 (Fig. 3). Given the geometric location of the end points P_1=[0,r_i] and P_2=[L,r_9+δ] and A_9/A_8, it is possible to specify different values of boattail closing angle β and generate a family of different afterbody geometries. Relative to the circular arc afterbody the new parametrization offers an increased degree of flexibility (

Fig**. 4** 4).

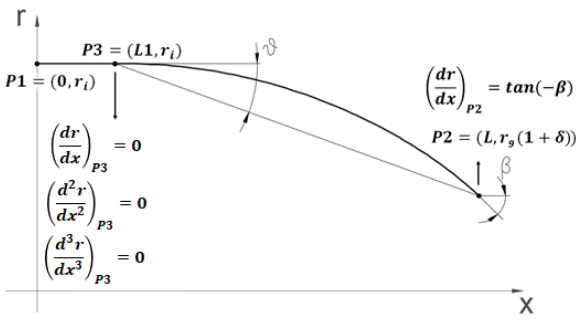


Fig. 2: Additional geometric constraint used to construct the afterbody geometry

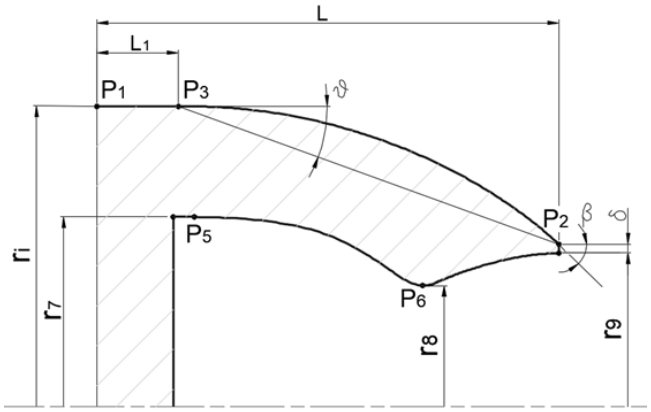


Fig. 3: Example of CST afterbody with ideal exhaust contour

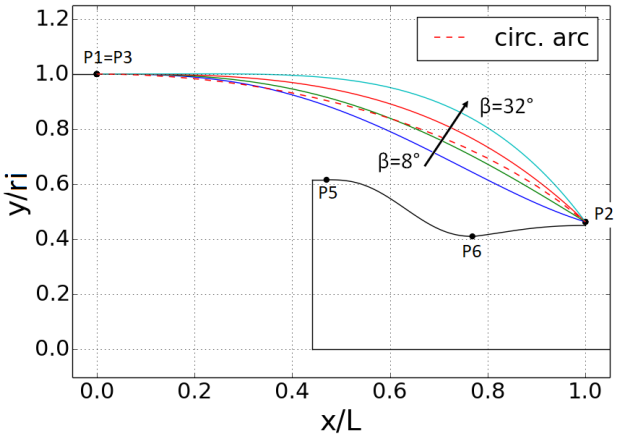


Fig. 4: Effect of β on the afterbody geometry parametrized using the CST method

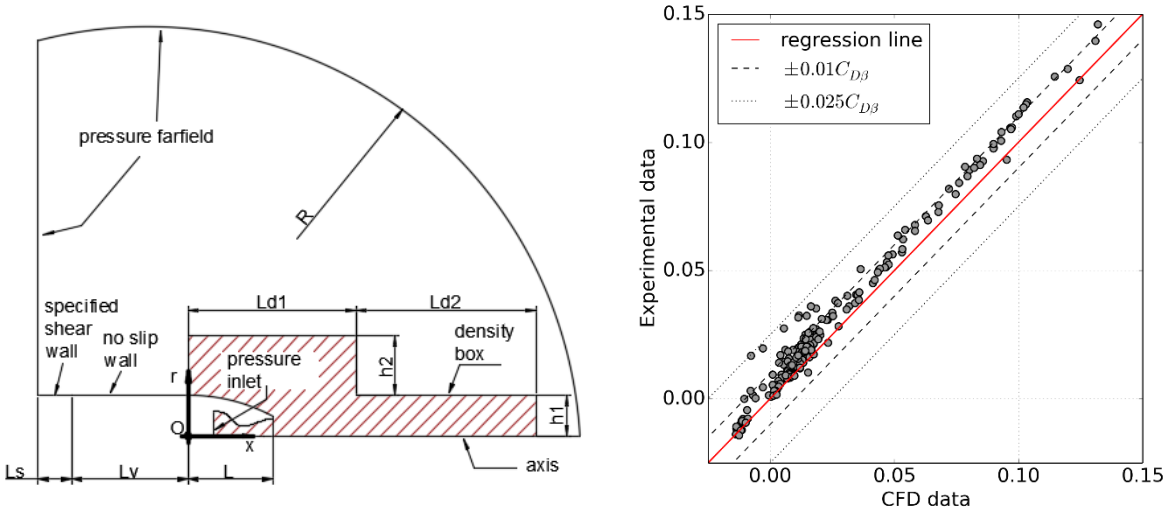
B. CFD Analysis

The afterbody aerodynamic data was generated using a steady CFD method. An implicit, density based, axisymmetric Favre Averaged Navier-Stokes (commonly referred as RANS) solver was used. The conservation equations were discretized with a second order scheme and the gradients were computed with a Green-Gauss node-based method. The axisymmetric computational domain was a truncated circular far-field of radius $80r_i$, a straight vertical inlet plane (Fig. 5), a symmetry axis (x-axis) and a sting that extends $22r_i$ upstream of the afterbody from the point $P_1=(0,r_i)$. The sting was modelled as inviscid adiabatic wall for the initial portion close to the far-field boundary ($Ls=6.6r_i$) and as a viscous adiabatic wall for the remaining part (Fig. 5a). All other walls were modelled as no-slip

adiabatic boundary conditions. On the circular bounds and inlet plane of the domain a pressure far-field boundary condition was applied where the static pressure and temperature were prescribed. The free-stream Mach number was altered by changing the total pressure at the far-field with static pressure and static temperature kept constant. The inlet of the nozzle duct was modelled with a pressure inlet boundary condition where the NPR was changed by prescribing the inlet total pressure.

The computational mesh was generated using a hybrid approach with rectangular cells in the boundary layer and an unstructured mesh of triangular cells in the remaining part of the domain. The boundary layer was discretized with a set of 60 inflation layers spaced with a growth ratio of 1.15 and a target y^+ of 1. The appropriate mesh size was assessed through a grid independence study based on the Grid Convergence Index (GCI) approach. This uses a constant refinement ratio [19], [20] for the different meshes. The GCI was computed based on C_D and three meshes of sizes 138, 444 and 1416 thousand elements. The GCI analysis was performed for two flight conditions: M_∞=0.8 and M_∞=1.4. The GCI index for the subsonic case was 0.4% between the coarse and medium mesh and 0.03% between the medium and the fine mesh based on C_D. For the supersonic case the GCI index was 0.8% between the coarse ad medium mesh and 0.02% between the medium and fine mesh. After this study, the medium mesh size of approximately 440 thousands elements was used.

The CFD approach was validated against experimental data [4] based on the performance of circular arc afterbodies. The afterbody pressure drag coefficient ($C_{D\beta}$) was calculated for approximately 75 combinations of M_∞ and power settings (NPR), ranging from M_∞=0.4 to $M_\infty = 1.3$ and NPR=1.4 to NPR=6.0. The CFD results generally correlate well with the experiments across the whole range for NPR, M_∞ and for all the different afterbody geometries (Fig. 5b). A statistical analysis of the difference shows that about 86% of the results computed with the CFD approach are within a difference band of $\pm 0.01 C_{D\beta}$.



(a) (b)

Fig. 5 (a) Computational domain and boundary conditions and (b) correlation between CFD and experimental $C_{D\beta}$ calculations

C. Geometric and Aerodynamic Configurations

To evaluate different aspects of axisymmetric afterbody and exhaust systems aerodynamic characteristics two Design Space Explorations (DSEs) are performed. These aim to quantify the effect of A_9/A_8, β, ϑ, NPR and M_∞ on afterbody drag, nozzle velocity coefficient and the overall balance of Net Afterbody Force (NAF). For the first study (DSE-1) three values of A_9/A_8 are chosen to study the effect of the operating conditions of variable area nozzles on afterbody drag (Fig. 6). A range of afterbody configurations are evaluated with β of 10,20, 30 degrees (Fig. 7b) and ϑ across the range 7-20 degrees. The value of ϑ depends on the independent parameter L_1 (Fig. 3) and A_9/A_8 (Fig. 7a). For all configurationss L, δ and A_8 are kept constant. Based on previous work [11] δ was specified as $0.03r_9$. The total number of geometries was 36 generated using a full factorial approach of the ranges reported in Table 1a. The NPR varies independently in the interval 3.5 to 8.25 with a step size of approximately 0.75 and including the design point NPR of the three area ratios chosen. To capture the sensitivity of the afterbody drag to M_∞ across the range 0.6-1.4

the sample space was based on a Prandtl-Glauert factor (β_1) spacing. For $M_\infty < 1$ the β_1 step size is 0.08 while for $M_\infty > 1$ the step size is 0.085. The external Reynolds number per unit of length varied from 3.3x10^6 to 7.5x10^6 depending on M_∞. All the cases are computed at 11km of altitude in ISA ambient conditions and T_7 is kept constant at 770K. The total number of aerodynamic conditions was 128, spaced using a full factorial approach Table 1b. Overall the combined geometric and aerodynamic dataset comprised 4608 CFD simulations for DSE-1.

The aim of the second DSE (DSE-2) was to assess the aerodynamic performance of afterbody and nozzle systems when operated at design point NPR (DNPR). This includes the same ranges of aerodynamic DoF explored in DSE-1. These are 3.5 to 8.25 for NPR and 0.6-1.4 for M_∞. The overall afterbody length L remains unchanged and so does the nozzle throat area A_8. β varies in the interval 10-30 degrees with a step size of 10 degrees, ϑ varies in the range 7-20 and the values of A_9/A_8 are a function of NPR. In this DSE each value of A_9/A_8 corresponds to design point area ratio for the given value of NPR and T_7. All the simulations take place at 11km of altitude in ISA ambient conditions and T_7 is kept constant at 770K. The number of aerodynamic conditions in DSE-2 is 128 (Table 2b) and the number of geometries is 12 (Table 2a), giving a total of 1536 cases spaced using a full factorial approach.

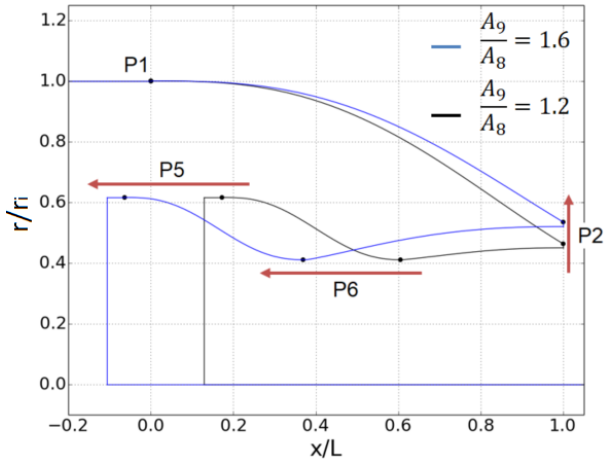
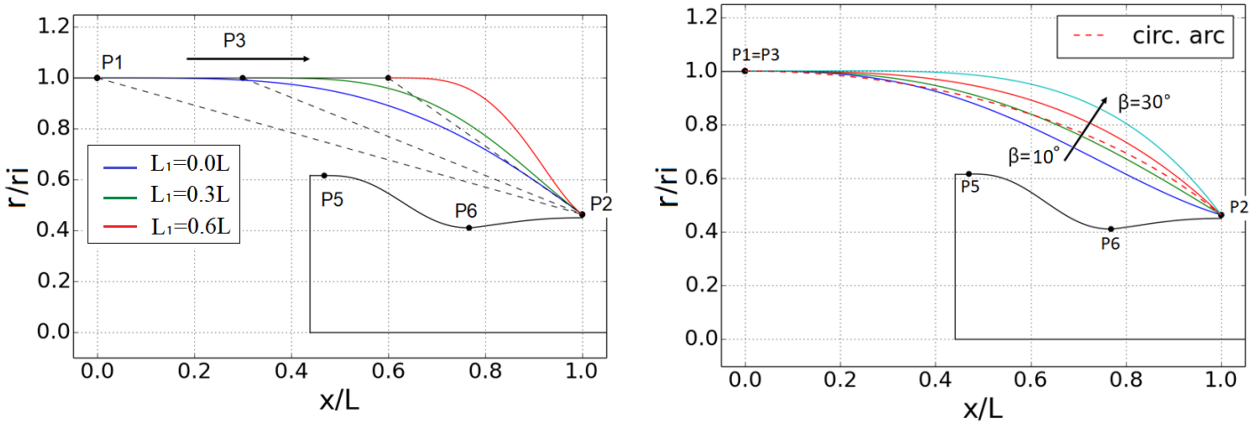


Fig. 6: Comparison of geometries for different values of A_9/A_8



(a) (b)

Fig. 7: Effect of (a) ϑ = [7°-19°] (b) β =[10°-30°] for a geometry with A8=1.2

DoF	Values
A_9/A_8	1.2, 1.4, 1.6
β	10°, 20°, 30°
L_1	0.0L, 0.2L, 0.4L, 0.6L
(ϑ)	(~5°-20°) *Dependent variable*

(a)

DoF	Range
NPR	3.5-8.25
M_∞	0.6-1.4

(b)

Table 1 (a) Geometric DoF and (b) Aerodynamic DoF for DSE-1

DoF	Values
A_9/A_8	function of NPR, range 1.16 to 1.782
β	10°, 20°, 30°
L_1	0.0L, 0.2L, 0.4L, 0.6L
(ϑ)	(~5°-20°) *Dependent variable*

(a)

DoF	Range
NPR	3.5-8.25
M_∞	0.6-1.4

(b)

Table 2: (a) Geometric DoF and (b) Aerodynamic DoF for DSE-2

D. Performance Metrics

The performance metrics are based on the stream force and control volume approach [21] and is defined following the schematics and engine station numbers of Fig. 8. The performance of the exhaust system is assessed through the velocity coefficient C_V (1), which is the ratio of the gross propulsive force at nozzle station 9 (F_9) over the ideal propulsive force (IPF). IPF is the ideal gross propulsive force that the nozzle would generate if the exhaust flow was ideally expanded to ambient conditions.

$$\boldsymbol{C_V = \frac{F_9}{IPF} = \frac{F_7 - \vartheta_{noz}}{IPF}} \tag{1}$$

Where F_7 is the momentum and pressure force at nozzle station 7, ϑ_{noz} is the pressure and shear force integrated along the internal nozzle walls from nozzle station 7 to station 9 (2).

$$\boldsymbol{\vartheta_{noz} = \int_{st.7}^{st.9} p dA\, \hat{n}_x + \int_{st.7}^{st.9} \tau_x dA} \tag{2}$$

IPF is defined as (3):

$$\boldsymbol{IPF = \dot{m}_{CFD} V_9^{ideal}} \tag{3}$$

Where $\dot{m}_{CFD}$ is the mass flow rate at station 7 while the ideal velocity at station 9 (V_9^{ideal}) is calculated using ideal, zero-dimensional gas dynamics. For a choked convergent divergent nozzle V_9^{ideal} is defined as:

$$V_9^{ideal} = \sqrt{\frac{2\gamma RT_7}{\gamma - 1}\left(1 - \left(\frac{1}{NPR}\right)^{\frac{\gamma-1}{\gamma}}\right)} \tag{4}$$

Where γ is the specific heat ratio, R is the gas constant for dry air. The metric used to assess the aerodynamic performance of the afterbody is the drag coefficient C_D. This accounts for the effect of the viscous and pressure forces acting on the external afterbody surface including the nozzle base region (5).

$$C_D = \frac{\phi_{aft}}{\frac{1}{2}A_1 V_\infty^2 \rho_\infty} \tag{5}$$

Where ϕ_{aft} is the external drag force, V_∞ is the free-stream velocity A_i is the shoulder cross section area and ρ_∞ is the free-stream density. The Net Afterbody Force (NAF) is defined as follows:

$$NAF = F_9 - \phi_{aft} \tag{6}$$

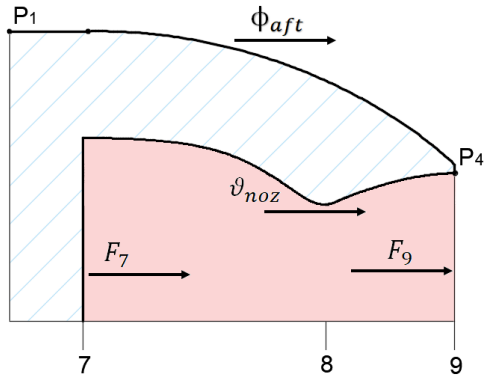


Fig. 8 Control volumes and forces definition for a generic afterbody and exhaust system

V.Results and Discussion

A. Aerodynamic Characteristics

1. Internal exhaust performance

The ideal internal nozzle contour is chosen to minimize the interaction effects between external afterbody surface and exhaust plume. This ensures that for a given a power setting (NPR, A_9/A_8) the nozzle performance remains unchanged regardless of M_∞ and the external afterbody geometry. The nozzle performance metric C_V is therefore well behaved and it only varies with NPR (Fig. 9) for the range of NPR and A_9/A_8 considered. To enable comparisons between C_D and C_V the forces (ϕ_{aft}, NAF and F_9) are normalized with respect to F_9 at the DNPR for each specified A_9/A_8. This enables the understanding of the trade off between thrust and drag forces for different afterbody geometries and flight conditions (M_∞).

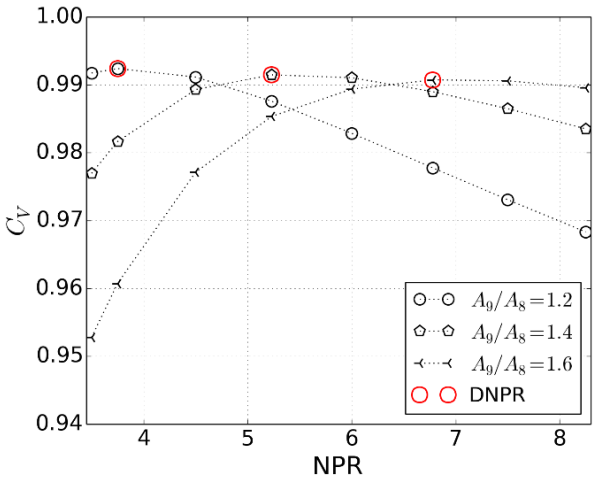


Fig. 9 C_V vs NPR for three values of A_9/A_8, β=20°, L1=0.0L, M_∞=1.0

2. External afterbody aerodynamic performance

The primary metric of interest is C_D which is dependent on the geometric (β, ϑ, A_9/A_8) and aerodynamic (NPR, M_∞) parameters. As expected M_∞ has a first order effect on C_D. Fig. 10 shows the effect of M_∞ and β and ϑ on C_D for a geometry with a given value of A_9/A_8 operated at its design point NPR (DNPR). For low values of ϑ (7°-8°), corresponding to L_1=0.0L, the afterbody external flow is more sensitive to changes in β due to the effect that this parameter has on the curvature distribution of the external contour line. When β is low (10°) the rate of change of the geometric gradient between P_1=(0,r_i) and P_2=(L,r_9+δ) (Fig. 3) is small which results in a smooth expansion of the external flow along the afterbody (Fig. 11a). As the value of β increases and the afterbody closing shape gets steeper the external flow accelerates. This results in a lower static pressure distribution along the afterbody and an increase in C_D (Fig. 11b). For larger values of ϑ (~16°-20°) the shape of the afterbody between P_3=(L_1,r_i) and P_2=(L,r_9+δ) has a marginal impact on C_D. Even though the value of β still controls the curvature distribution (dr^2/d^2x) along the afterbody the rate of change of the geometrical gradient is greater to allow the CST line to reach P_2 in a reduced length (L-L_1). This causes the external flow to separate right after P_3 (Fig. 12) making the afterbody drag insensitive to changes in β.

The off design operation of the exhaust impacts the flow topology downstream of nozzle station 9 and therefore it affects the shape of the post exit stream tube. The static pressure distribution along the afterbody at a given flight condition (M_∞) and for a given afterbody external geometry (β, ϑ) is affected by the shape of the post exit stream tube. For a fixed value of ϑ, operating the nozzle in the under-expanded region always has a beneficial effect on C_D. For example, a geometry with A_9/A_8=1.2, β=10° and ϑ=10° at M_∞=1.0 has a 15% reduction in C_D if NPR is increased from 3.75 (DNPR) to NPR=8.25 (Fig. 13). This happens because the oblique shock at nozzle station 9 gets stronger and consequently there is an increase in the static pressure of the exhaust plume (Fig. 14). As the static pressure in the exhaust plume increases, so does the static pressure on the external afterbody line and thereby it reduces C_D. For the over-expanded case the position of the shock on the external afterbody is not dependent on NPR. However, a geometry with A_9/A_8=1.4 (DNPR=5.23), β=30° and ϑ=14° at M_∞=1.0 has a 6% reduction in C_D if NPR is decreased from 5.23 (DNPR) to NPR=3.5 (Fig. 15). The cross section of the stream tube reduces as NPR reduces affecting the shape of the separated region in the aft end of the external afterbody line. This changes the effective afterbody geometry and it affects the strength of the shock on the external afterbody shoulder. For example, for a geometry with A_9/A_8=1.4 (DNPR=5.23) (Fig. 15a), β=30° and ϑ=14° at M_∞=1.0 the pre-shock Mach number is 1.41 when the exhaust is operated at DNPR while it is 1.39 when the exhaust is operated at NPR=3.5 (Fig. 15b). This changes the flow expansion on the shoulder resulting in a lower static pressure distribution for the case with the higher pre-shock Mach number. In this case the afterbody drag reduces by 6%.

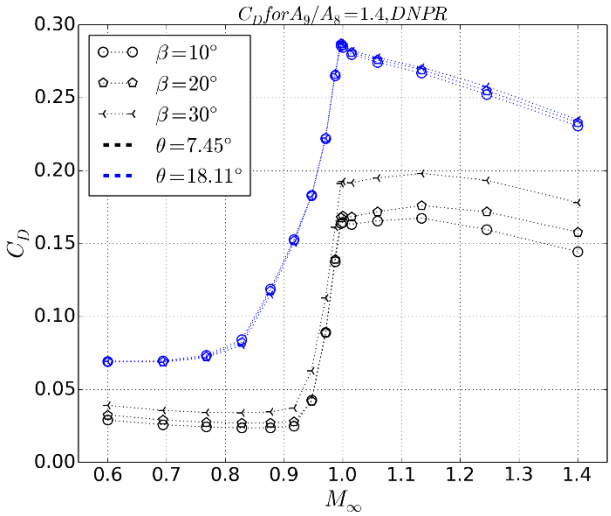
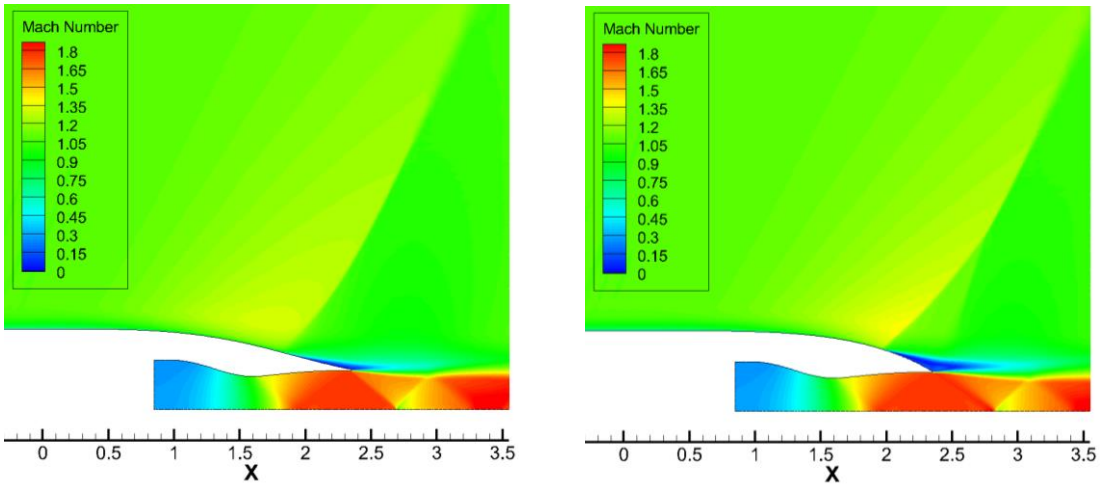
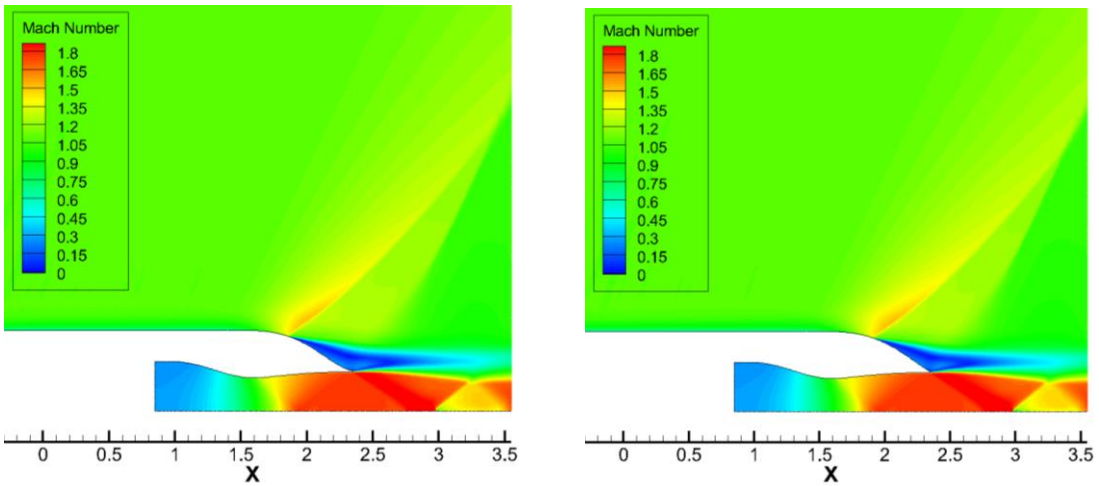


Fig. 10:C_D lines for different values of β and ϑ



(a) (b)

Fig. 11: Effect of β for NPR=DNPR, ϑ=7.45°, A9/A8=1.4 and M_∞ =1.059 - (a) β=10° and (b) β=30°



(a) (b)

Fig. 12: Effect of β for NPR=DNPR, ϑ=18.11°, A9/A8=1.4 and M_∞ =1.059 - (a) β=10° and (b) β=30°

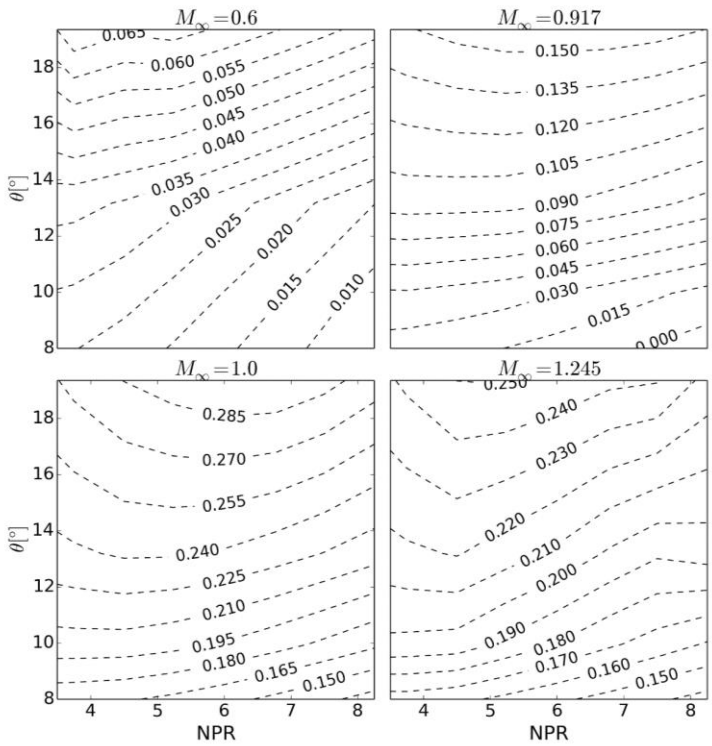
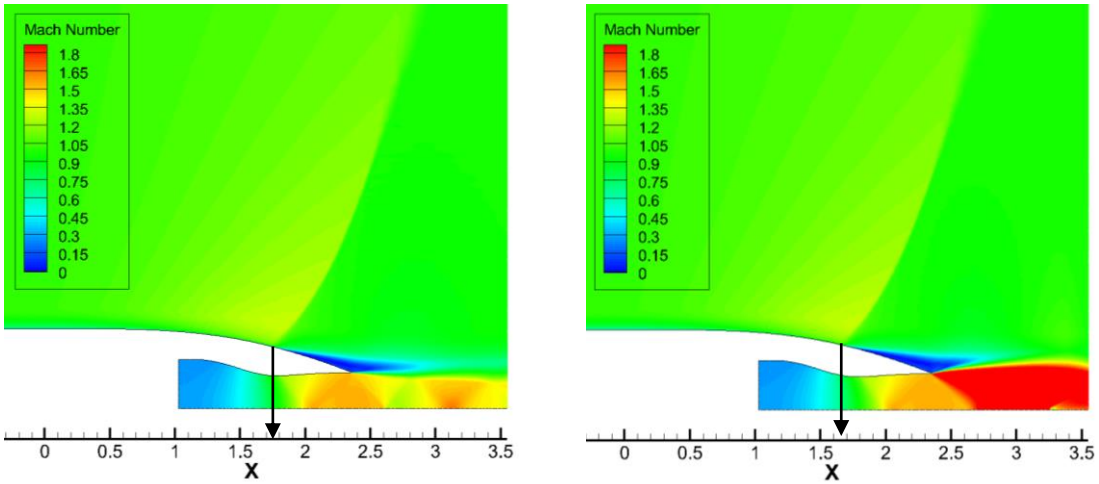


Fig. 13:C_D iso lines – A_9/A_8=1.2 β=10°



(a) (b)

Fig. 14: Effect of NPR for β=20°, ϑ=8.0°, A9/A8=1.2 and M_∞ =0.997 - (a) DNPR (b) NPR=8.25

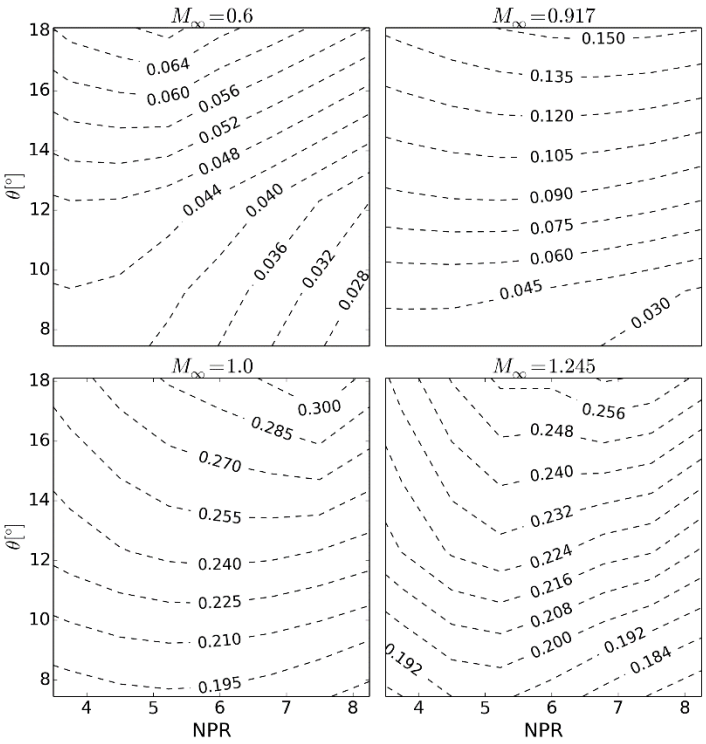


Fig. 15: C_D iso lines – A_9/A_8=1.4 β=30°

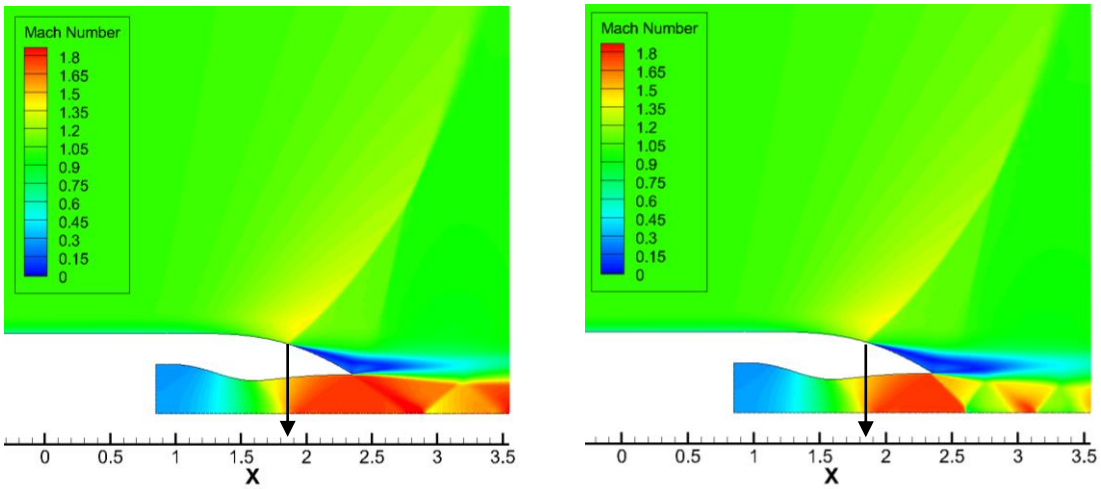


Fig. 16: Effect of NPR for β=30°, ϑ=12.3°, A9/A8=1.4 and M_∞ =1.0 - (a) DNPR (b) NPR=3.5

3. *Overall afterbody and nozzle system performance*

Even though performance metrics such as C_D are useful for preliminary design assessments, it does not consider the combined effect of afterbody and nozzle system designs. For instance, for a given geometry (Fig. 9, Fig. 13) as NPR increases both exhaust C_V and afterbody drag C_D are decreasing. In the context of preliminary design, it is useful to normalize all the forces (ϕ_{aft}, NAF and F_9) with the same value to understand the trade-off between the thrust domain and the drag domain. In the first instance drag and net afterbody force (NAF) are non-dimensionalised with F_9 at DNPR for a given value of A_9/A_8. D_N and NAF_N are defined as $\phi_{aft}/F_9(DNPR)$ and $NAF/F_9(DNPR)$ respectively.

Fig. 17 shows the effect of β and ϑ on the normalized drag (D_N) force ($\phi_{aft}/F_9(DNPR)$) for a specified value of A_9/A_8 and M_∞. For small values of ϑ the shape of the rear end of the afterbody has an effect on its aerodynamic performance. For ϑ=8.0°, A9/A8=1.2 and M_∞=1.0 an increase in β from 10° to 30° accounts for approximately a 20% increase in D_N relatively to the geometry with β=10° operated at DNPR condition. For a given β=20° an increase in ϑ from 8° to 19° accounts for up to a 70% increase in D_N The afterbody drag is less sensitive to NPR where for the more benign configuration of ϑ=8° D_N reduces by about 23% when NPR increases from the DNPR of 3.75 to 8.25. Conversely, for the more aggressive afterbody configurations with a relatively high mean angle (ϑ=19°) D_N increases by up to 10% when NPR increases from the DNPR of 3.75 to a NPR of 6. An increase in A_9/A_8, for a given value of A_8, corresponds to an increase in F_9 at DNPR and generally lower values of D_N (Fig. 18, Fig. 19). However, the relative effect of each DoF remains broadly unchanged: for small values of ϑ the effect of an increase in β results in approximately a 30% increase in D_N while increasing NPR from 3.75 to 8.25 accounts for a 20% reduction in D_N. The largest effect is similarly due to a change in ϑ. An increase in ϑ from 7° to 17° corresponds to up to an 80% increase in D_N.

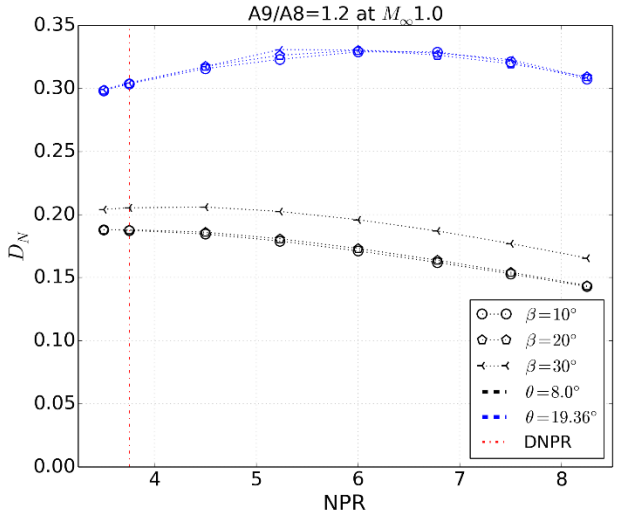


Fig. 17: effect of β, ϑ and NPR on D_N for A_9/A_8=1.2 and M_∞=1.0

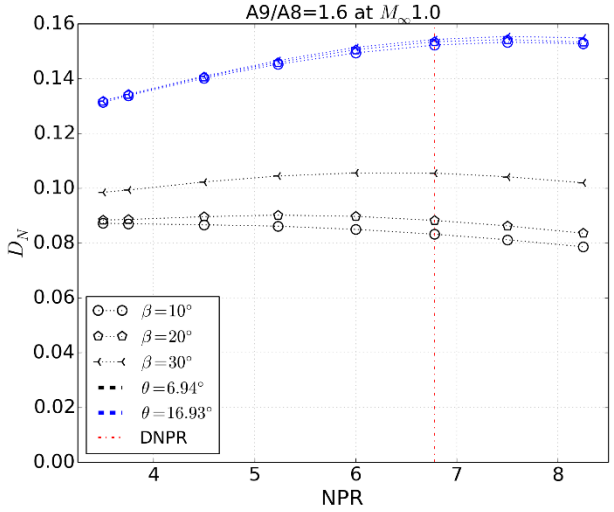


Fig. 18: effect of β, ϑ and NPR on D_N for A_9/A_8=1.6 and M_∞=1.0

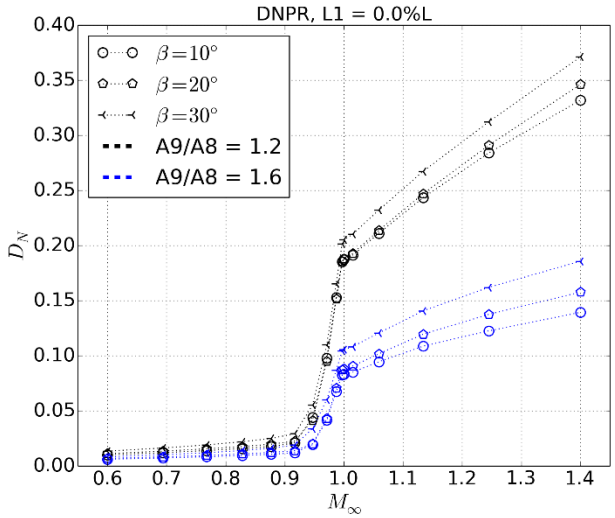
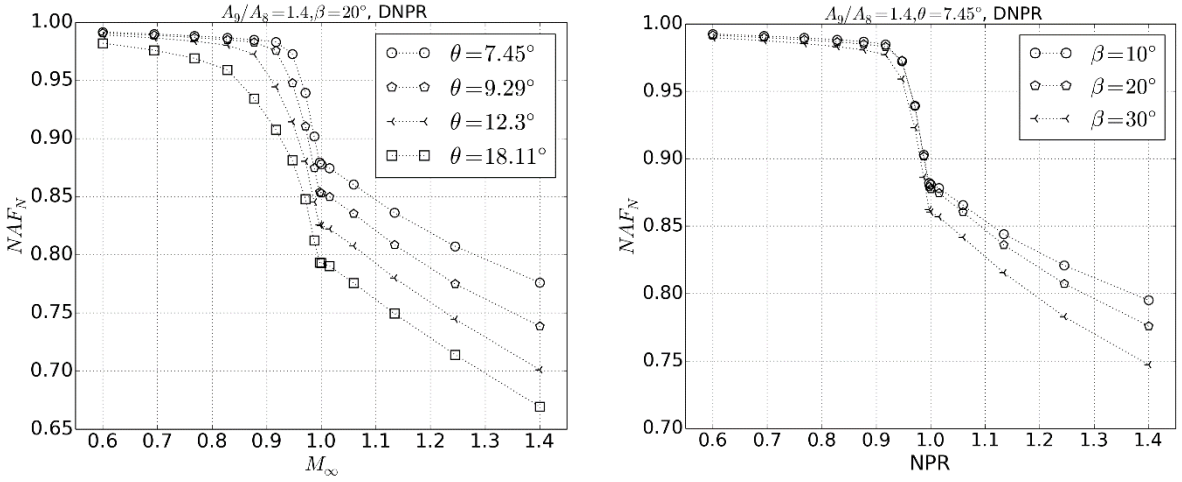


Fig. 19: effect of β and A_9/A_8 on D_N for NPR=DNPR ϑ=8°for A_9/A_8=1.2 and ϑ=7° for A_9/A_8=1.6

The combined effect of the afterbody drag and exhaust thrust is evaluated using the normalized net afterbody force (NAF_N), which is the NAF relative to F_9 at DNPR ($NAF/F_9(DNPR)$). This quantifies how much the forward propelling force is relatively to the GPF at DNPR for a specified afterbody geometry and a specified throttle setting (NPR). For instance, for a geometry with A_9/A_8=1.4, β=20° operated at DNPR an increase in ϑ from 7.45° to 18° accounts for about a 12.5% reduction in NAF_N at $M_\infty = 1.4$ (Fig. 20a). On the other hand, for an afterbody and nozzle system with A_9/A_8=1.4, ϑ=7.45° operated at its DNPR (5.23) an increase in β from 10° to 30°can lead to a 7% reduction in NAF_N at M_∞=1.4 (Fig. 20b). For larger A_9/A_8 the NAF_N values are progressively smaller as M_∞ due to the increase in F_9(DNPR) (Fig. 21b, c) while the opposite happens for smaller A_9/A_8 (Fig. 21a).



(a) (b)

Fig. 20: (a)effect of ϑ and (b) effect of β on NAF_N for A_9/A_8=1.4 at DNPR

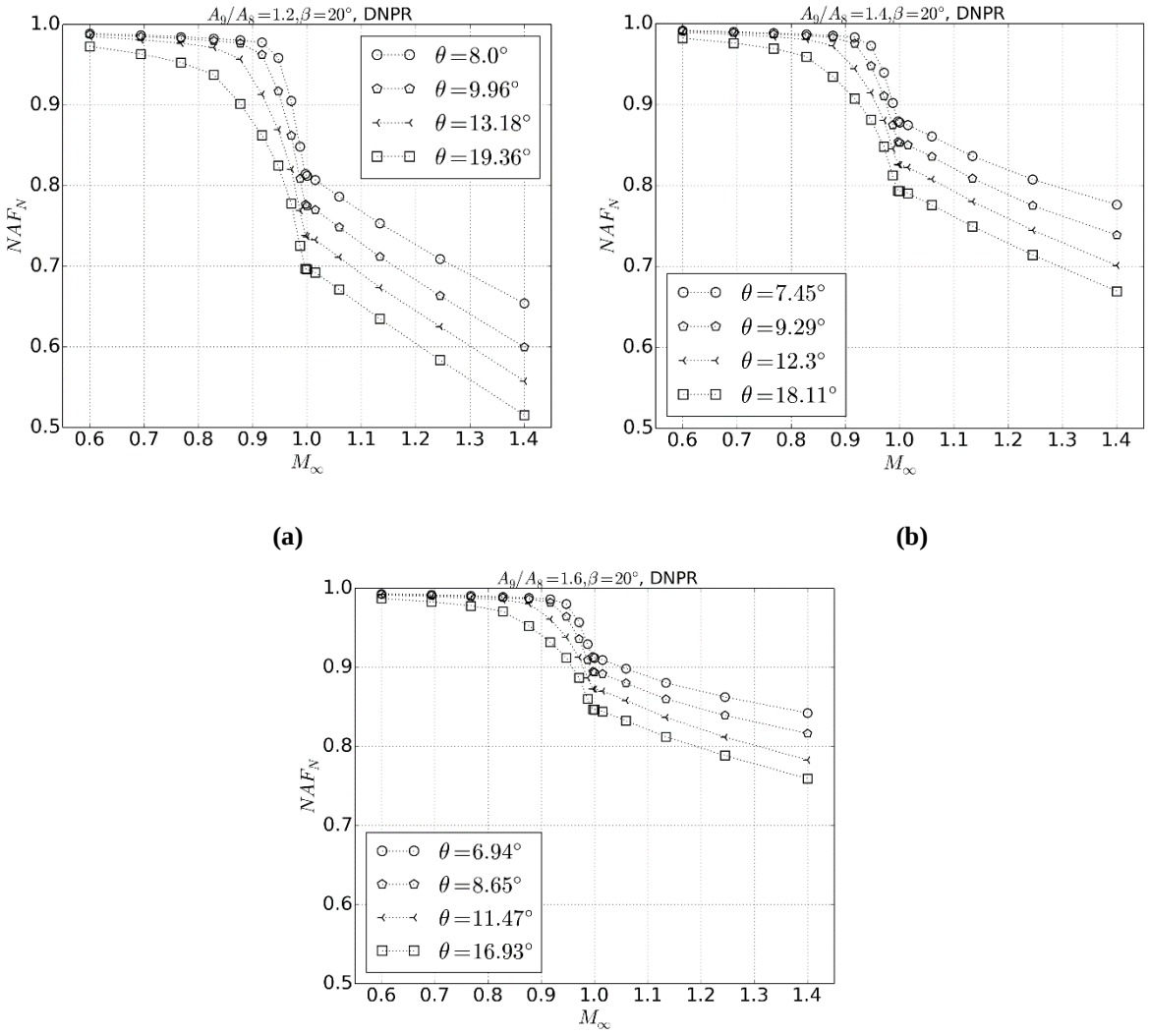
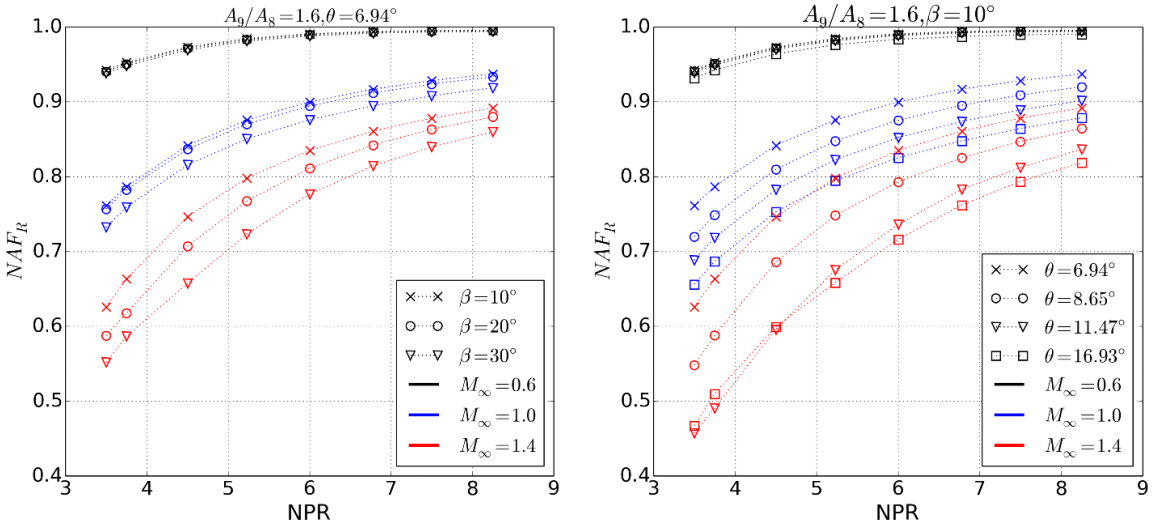


Fig. 21: Effect of ϑ on NAF_N for (a) A_9/A_8=1.2, (b) A_9/A_8=1.4 and (c) A_9/A_8=1.6 at DNPR

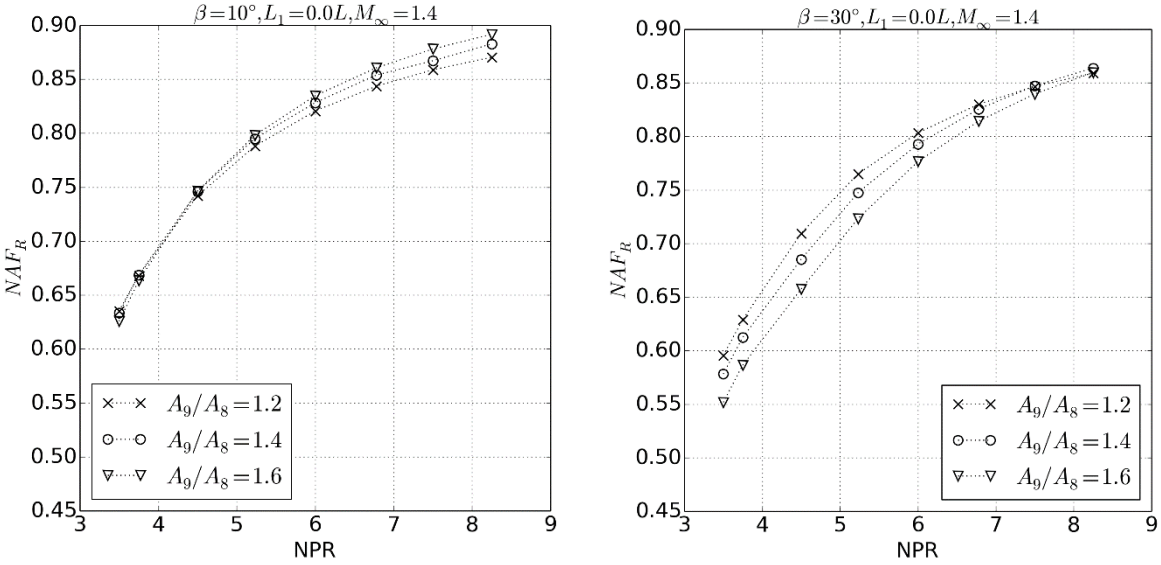
For preliminary design purposes it is important to understand how all the forces acting on an afterbody and nozzle system compare with the maximum thrust achievable for a given geometry at a given operating condition. For this purpose NAF_R is defined as $NAF_R = NAF/(F_{9max}(NPR))$. $F_{9max}(NPR)$ is defined as the F_9 produced by a geometry that has a given NPR as DNPR. This is the maximum F_9 achievable with an ideal exhaust contour at a certain NPR. This quantifies how much of the maximum achievable forward propelling force for a given NPR is lost due to the combination of afterbody and exhaust geometry and M_∞. Since for the idealized exhaust contour C_V at DNPR is not dependent on any of the geometry or on M_∞ this normalization can be used across the DSE results. This combines the data obtained from DSE-1 and DSE-2. For a geometry with A_9/A_8=1.6 and ϑ=6.94° an increase in β from 10° to 30° reduces NAF_R by up to 15% across the range of NPR from 3.5 to 8.25. For the same geometry (A_9/A_8=1.6 and ϑ=6.94°) at a given value of β=20° when NPR is decreased from 8.25 to 3.5 there is a 35% reduction in NAF_R relative to the maximum NPR value at M_∞.=1.4 (Fig. 22a). The effect of an increase in ϑ from 6.94° to 16.93° is up to a 31% reduction in NAF_R (Fig. 22b). The effect of different values of A_9/A_8 on NAF_R is relatively small for geometries with small ϑ (or L_1). In the case of a geometry with β=10° the effect of increasing A_9/A_8 from 1.2 to 1.6 is relevant only for large values of NPR and it accounts for a 5% increase in NAF_R relatively to A_9/A_8 =1.2 (Fig. 23a). For a geometry with β=30° the effect of an increase in the value of A_9/A_8 is relevant only for low values of NPR and it accounts for an 8% increase in NAF_R relatively to A_9/A_8 =1.6 (Fig. 23b). For

geometries with larger ϑ NAF_R is insensitive to changes in A_9/A_8 and β (Fig. 24a). For lower M_∞ the NAF_R curves move to higher values (Fig. 24b).



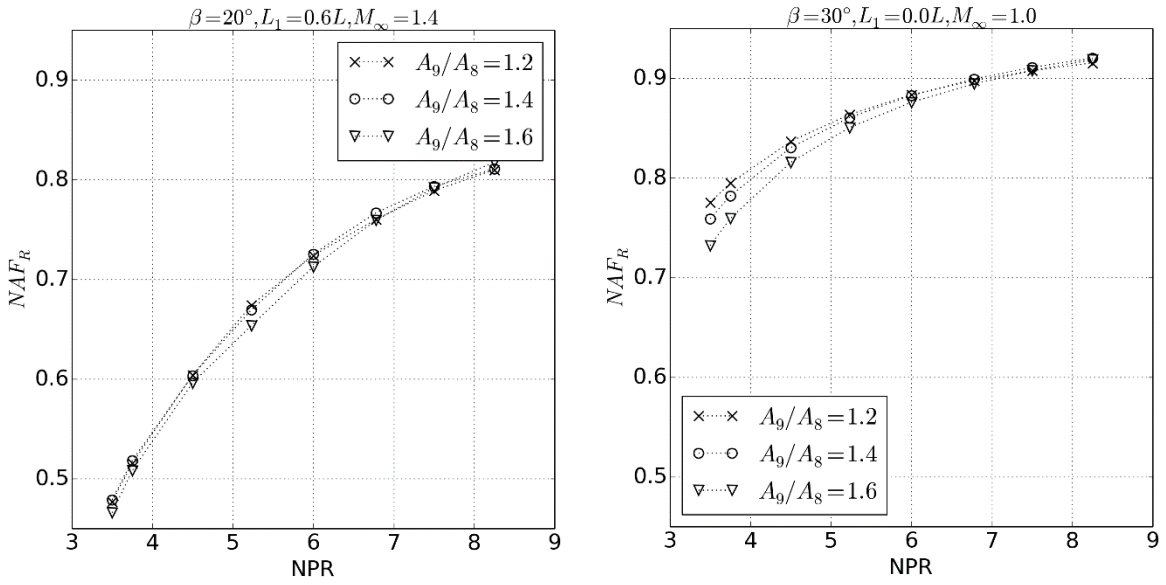
(a) (b)

Fig. 22: (a)effect of NPR, β, M_∞ on NAF_R, ϑ=6.94° and (b) effect of ϑ, NPR, M_∞ on NAF_R, β=10°



(a) (b)

Fig. 23: effect of A_9/A_8 and NPR on NAF_R for (a) β=10° and (b) β=30°



(a) (b)

Fig. 24: effect of A_9/A_8 and NPR on NAF_R for (a) β=20°, L_1=0.6L M_∞=1.4 and (b) β=30°, L_1=0.0L M_∞=1.0

VI.Conclusions

This research has quantitatively assessed the impact of axisymmetric afterbody geometry and nozzle system aerodynamic performance under a range of flight conditions (M_∞) and throttle settings (NPR). The key factor that enabled this work to develop was a novel external afterbody geometry parametrization based on the CST method. This proved more flexible than the conventional parametrizations and allowed the exploration of three main geometric DoF: afterbody mean angle (ϑ), boattail closing angle (β) and nozzle exit to throat area ratio (A_9/A_8). Based on this work it can be concluded that:

- ϑ has a relevant impact on C_D. An increase in the value of ϑ from 7° to 20°can increase C_D by 80%. ϑ has a large impact on both NAF_N and NAF_R. An increase in ϑ can reduce NAF_N by 12.5% and NAF_R by approximately 30%.
- β has an impact on the afterbody drag only when the external flow undergoes a smooth expansion around the external afterbody shoulder. This happens for small values of ϑ. An increase in β from 10° to 30° can cause up to a 25% increase in C_D and up to a 8% decrease in NAF_N. The decrease in NAF_R due to an increase in β can be up to 15%.
- NPR affects the shape of the exhaust stream tube. This affects the position of the shock on the afterbody external surface as well as the shape of the separated region close to its aft end. Both over-expanded and under-expanded operating conditions result in up to a 15% reduction in C_D. Increasing NPR from 3.5 to 8.25 is beneficial for NAF_R especially at supersonic M_∞ where the NAF_R improvement can be up to 50%.

References

[1] D. Cler, "A parametric investigation of nozzle planform and internal /external geometry at transonic speeds," in *31st Joint Propulsion Conference and Exhibit*, 1995.

[2] D. E. Reubush and J. F. Runckel, "Effect of Fineness Ratio on Boattail Drag of Circular-Arc Afterbodies Having Closure Ratio of 0.50 With Jet Exhaust at Mach Numbers up to 1.30," NASA TN D-7192, Hampton, Virginia, 1973.

[3] P. R. Payne, R. M. Hartley, and R. M. Taylor, "Afterbody Drag: Volume 1 - Drag of Conical and Circular Arc Afterbodies without Jet Flow," Bethesda, Maryland, 1980.

[4] D. E. Reubush, "Effect of Fineness and Closure Ratios on Boattail Drag of Circular-Arc Afterbody Models With Jet Exhaust at Mach Numbers up to 1.30," NASA TN D-7163, Hampton, Virginia, 1973.

[5] G. Carson and E. E. Lee, "Experimental and Analytical Investigation of Axysimmetric Supersonic Cruise

Nozzle Geometry at Mach Numbers From 0.60 to 1.30," NASA TP-1953, Hampton, Virginia, 1981.
[6] G. S. Pick and R. M. Hartley, "Afterbody Drag Volume 3 - Literature Survey," Bethesda, Maryland, 1980.
[7] R. Christie, A. Heidebrecht, and D. MacManus, "An Automated Approach to Nacelle Parameterization Using Intuitive Class Shape Transformation Curves," *J. Eng. Gas Turbines Power*, vol. 139, no. 6, 2017.
[8] B. M. Kulfan, "'CST' Universal Parametric Geometry Representation Method With Applications to Supersonic Aircraft," *J. Aircr.*, vol. 45, no. 1, 2008.
[9] Royal Aeronautical Society, "Subsonic pressure drag of boat-tails with negligible annular base area in the presence of a central propulsive jet," ESDU 01012, 2001.
[10] Langley Research Center, "NASA TM-102750 - A User's Guide to the Langley 16-Foot Transonic Tunnel Complex," Hampton, Virginia, 1990.
[11] L. E. Putnam and C. E. Mercer, "Pitot-Pressure Measurements in Flow Field Behind a Rectangular Nozzle With Exhaust Jet for Free-Stream Mach Numbers of 0.00, 0.60, and 1.20," NASA TM-88990, Hampton, Virginia, 1986.
[12] H. Chen, U. Navier, S. Computation, Y. Zhang, and H. Chen, "Performance Prediction of Conical Nozzle using Navier-Stokes Computation Performance Prediction of Conical Nozzle," *J. Propuls. Power*, vol. 31, no. 1, pp. 192–203, 2015.
[13] J. R. Debonis, N. J. Georgiadis, and C. F. Smith, "Validation of the NPARC Code for Nozzle Afterbody Flows at Transonic Speeds," NASA TM 106971, 1995.
[14] R. G. M. Hasan, J. J. McGuirk, D. D. Apsley, and M. A. Leschziner, "A turbulence model study of separated 3D jet/afterbody flow," *Aeronaut. J.*, vol. 108, no. 1079, 2004.
[15] J. D. Anderson, *Modern Compressible Flow With Historical Perspective*, Second Ed. McGraw-Hill, 1990.
[16] A. H. Shapiro, *The Dynamics and Thermodynamics of Compressible Fluid Flow*. New York: The Ronald Press Company, 1954.
[17] T. Zebbiche, "Supersonic axisymmetric minimum length nozzle conception at high temperature with application for air," *KSAS Int. J.*, vol. 9, no. 1, pp. 1–30, 2008.
[18] B. M. Agrow and G. Emanuel, "Comparison of minimum length nozzles - Agrow, B. M..pdf," *J. Fluids Eng.*, vol. 110, pp. 283–288, 1988.
[19] P. J. Roache, "Perspective: A Method for Uniform Reporting of Grid Refinement Studies," *J. Fluids Eng.*, vol. 116, pp. 405–413, 1994.
[20] F. Elizalde-Blancas and P. J. Roache, "An Evaluation of the GCI for Unstructured Grids."
[21] AGARD 237, "Guide to In-Flight Thrust Measurement of Turbojets and Fan Engines," 1979.



https://dspace.org/

Geometry parametrization and aerodynamic characteristics of axisymmetric afterbodies

Zuccolo, Giovanni; MacManus, David G.; Goulos, Ioannis; Martin, Peter

2020-01-05
AIAA
https://doi.org/10.2514/6.2020-2222
Zuccolo G, MacManus D, Goulos I, Martin P (2020) Geometry parametrization and aerodynamic characteristics of axisymmetric afterbodies. In: 2020 AIAA SciTech Forum, 6-10 January 2020 Orlando, Florida

Downloaded from a DSpace repository. https://dspace.org/